

Learning eigenstates of quantum many-body Hamiltonians within the symmetric subspaces using neural network quantum states

Shuai-Ting Bao,¹ Dian Wu,² Pan Zhang,³ and Ling Wang^{1,*}

¹*School of Physics, Zhejiang University, Hangzhou 310058, China*

²*Institute of Physics, École Polytechnique Fédérale de Lausanne (EPFL), CH-1015 Lausanne, Switzerland*

³*CAS Key Laboratory for Theoretical Physics, Institute of Theoretical Physics, Chinese Academy of Sciences, Beijing 100190, China*

(Dated: August 12, 2024)

The exploration of neural network quantum states has become widespread in the studies of complicated quantum many-body systems. However, achieving high precision remains challenging due to the exponential growth of Hilbert space size and the intricate sign structures. Utilizing symmetries of the physical system, we propose a method to evaluate and sample the variational ansatz within a symmetric subspace. This approach isolates different symmetry sectors, reducing the relevant Hilbert space size by a factor approximately proportional to the size of the symmetry group. It is inspired by exact diagonalization techniques and the work of Choo et al. in Phys. Rev. Lett. **121**, 167204 (2018). We validate our method using the frustrated spin- $\frac{1}{2}$ J_1 - J_2 antiferromagnetic Heisenberg chain and compare its performance to the case without symmetrization. The results indicate that our symmetric subspace approach achieves a substantial improvement over the full Hilbert space on optimizing the ansatz, reducing the energy error by orders of magnitude. We also compare the results on degenerate eigenstates with different quantum numbers, highlighting the advantage of operating within a smaller Hilbert subspace.

Introduction. The advancement of neural quantum state (NQS) has been impressive since its initial development, and numerous established models have been successfully applied to solve challenges in quantum many-body systems. Notable ones among these models include the convolutional neural network (CNN) [1, 2], the graph neural network (GNN) [3–6], the recurrent neural network (RNN) [7], and the transformer [8, 9], each demonstrating remarkable achievements. The success of these models owes to their properties that align closely with well-known physical concepts. For instance, CNNs explicitly incorporate translational invariance, and the graph attention mechanism in GNNs resembles the coarse-graining properties of tensor network states [10]. However, despite these advancements, the complexity of quantum many-body wave functions remains a formidable obstacle, attributed to the exponentially large Hilbert space and the lack of information regarding their sign structure.

Symmetry plays a crucial role in the design of variational ansatzes, which rules out physically improper states and serves as a guidance in variational optimization. Various methods have been proposed to integrate the physical symmetries into neural networks. For example, the CNN effectively captures the translational symmetry, but its applicability is confined to ground state simulations in the trivial symmetry sector, rendering it unsuitable for other symmetries such as reflections, rotations, and sublattice translations. The group convolutional network (GCN) [11] explicitly preserves the whole symmetry group of the Hamiltonian, but encounters scalability challenges due to the proportional increase in the number of variational parameters with the size of the symmetry group, which in turn scales with the system size. The discrete symmetries can also be imposed through a superposition of the corresponding symmetry-transformed basis components [1, 8, 9, 12]. However, without reducing the Hilbert space size, such superposed ansatzes still result in a computa-

tional complexity proportional to the size of the incorporated symmetry group.

There are several celebrated examples of incorporating symmetries non-trivially into variational ansatzes. For instance, in a manner analogous to the $SU(2)$ symmetric matrix product state (MPS), Vieira et al. [13] have used spin fusion quantum numbers as a sequence of variables and employed a restricted Boltzmann machine (RBM) to express the weights for the fusion path. In this approach, the input neurons are not local physical states but represent a global fusion path, thus preserve the non-abelian $SU(2)$ symmetry without the need of an additional z orientation to define the computational basis.

Choo et al. [14] have explored the translational symmetry by enforcing the amplitudes of translation-related real-space states to be identical while tracking the relative phases required by the symmetry sectors. This approach avoids the computational complexity of enumerating all group elements, and is capable of exploring low-energy excitations at different momenta. Although represented in the full Hilbert space, the way it imposes the symmetry is closely related to the construction of symmetric subspace commonly used in exact diagonalization (ED) under lattice symmetries and other conservation laws [15–19]. Subsequently, in full summation rather than sampling, Bukov et al. [20] have proposed to enumerate the basis reduced to the ground state symmetry sector, and further sum over all elements in the symmetry group to guide the optimization.

Building upon these advancements, we have developed an algorithm that integrates efficient enumeration or sampling of configurations with symmetric subspace construction, which offers several key advantages: The integration of symmetries results in a larger gap between the ground state and the lowest excited state within the subspace, facilitating faster convergence of the variational optimization. The non-local nature of

the symmetric basis vectors enhances the expressibility of the ansatz. Moreover, the significantly reduced size of the Hilbert space allows using smaller neural networks and fewer Monte Carlo samples to achieve satisfactory accuracy.

Method. Similar to the symmetric basis construction in ED methods, we construct a set of orthogonal basis vectors by the superposition of symmetry-transformed Ising basis $|a\rangle = |s_1 \otimes s_2 \otimes \dots \otimes s_N\rangle$, where N is the system size. Taking the translational symmetry in one dimension as an example, a symmetric basis vector is defined as follows [15–19]:

$$|a_k\rangle = \frac{1}{\sqrt{N_a}} \sum_{r=0}^{N-1} e^{-ikr} T^r |a\rangle, \quad (1)$$

where T is the operator that translates the local state by one lattice site and $\sqrt{N_a}$ is the normalization coefficient. This construction is generalizable to other dimensions and symmetry groups. The unique representative state $|a\rangle$ is the minimum one among the equivalence class $\{T^r |a\rangle\}$ for $r \in \{0, \dots, N-1\}$ encoded in the binary format, with 1 denoting $|\uparrow\rangle$ and 0 denoting $|\downarrow\rangle$. Given the quantum number k , any state $|\psi\rangle$ can be expressed in terms of the symmetric basis vectors $\{|a_k\rangle\}$:

$$|\psi\rangle = \sum_{a \in \{\text{repr. state}\}}^{N_{\text{repr}}} \psi(a) |a_k\rangle, \quad (2)$$

where N_{repr} is the size of the symmetric subspace. It is significantly reduced compared to the full Hilbert space due to the symmetry and the enforced orthogonality. The representative state $|a\rangle$, viewed as real-space physical neurons, is input into a neural network to retrieve the wave function coefficient $\psi(a)$. In this framework, no extra computational effort is required beyond enumerating or sampling representative configurations a , computing the matrix elements $\langle a_k | H | a'_k \rangle$, and evaluating the wave function coefficients $\psi(a)$. The matrix elements in the symmetric subspace can be computed efficiently, as usually adopted in ED methods [15–19].

Wave function ansatz. The architecture of NQS plays a crucial role in the wave function ansatz. Apart from the abundant available models, the methodologies for designing complex-valued wave functions are equally significant. We explore two distinct approaches: employing a network with complex parameters, referred to as ComplexNet throughout this paper; or employing two independent networks with real parameters to model the amplitude and phase separately, referred to as SeparateNet.

We use the most generic and effective neural network model, the feed-forward neural network (FFNN), to implement the two approaches and compare their accuracy and efficiency. The network outputs the logarithm of the wave function components, written as $\ln \psi(a) = \Psi(a)$. For ComplexNet, the output is a complex number $\Psi(a)$, i.e.,

$$\ln \psi(a) = \text{Re}\Psi(a) + i\text{Im}\Psi(a). \quad (3)$$

For SeparateNet, the two real networks output $A(a)$ and $\Phi(a)$ respectively, and we have

$$\ln \psi(a) = A(a) + i\Phi(a). \quad (4)$$

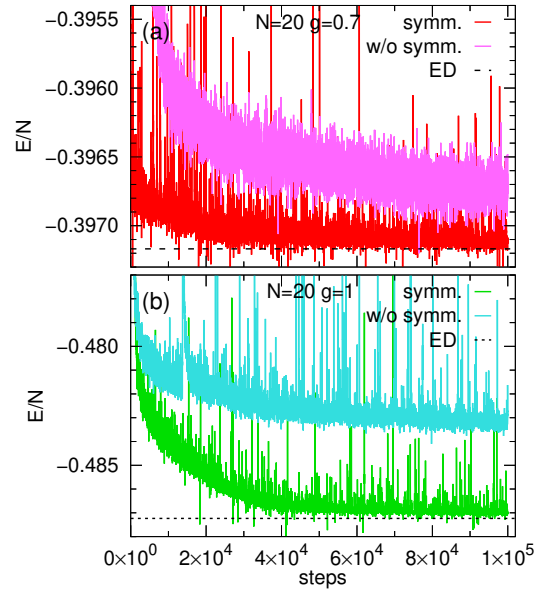


Figure 1. Ground state energy vs. optimization steps for the J_1 - J_2 chain of length $N = 20$ at (a) $g = 0.7$ and (b) $g = 1$, using Metropolis sampling. The NQS is a 4-layer complex FFNN with $\alpha_i = 2$. We compare the results with symmetrization to those with the same network and optimization strategy but without symmetrization.

Formally, $e^{\text{Re}\Psi(a)}$ (or $e^{A(a)}$) represents the amplitude, and $\text{Im}\Psi(a)$ (or $\Phi(a)$) represents the phase of the component $|a_k\rangle$ for a ComplexNet (or SeparateNet). For a FFNN with three layers as an example, we parameterize it in the following:

$$\ln \psi(a) = \mathbf{W}_3 f(\mathbf{W}_2 f(\mathbf{W}_1 a + \mathbf{b}_1) + \mathbf{b}_2), \quad (5)$$

where \mathbf{W}_i represents the weight matrix and \mathbf{b}_i represents the bias, whose values are complex (or real) for ComplexNet (or SeparateNet). The function f is a nonlinear activation function, for which we simply use the ReLU function in this work. The final weight matrix \mathbf{W}_3 is a row vector, which outputs a scalar after the matrix-vector multiplication. The number of hidden neurons at the i -th layer is denoted as $N_{h_i} = \alpha_i N$. The complex ReLU function is implemented by separately applying ReLU to its real and imaginary parts. The energy gradients and the stochastic reconfiguration (SR) [21–25] method to precondition the gradients are presented in the supplementary material [26].

Metropolis sampling algorithm. To sample a given probability distribution $p(a) = e^{2\text{Re}\Psi(a)}$ of configurations a , the Metropolis sampling must satisfy the detailed balance condition [27]:

$$p(a)g(a, a') = p(a')g(a', a), \quad (6)$$

where $g(a, a')$ is the proposed transition probability from a to $a' \neq a$. It ensures that at equilibrium, the number of transitions from a to a' equals the number of transitions from a' to a . We define $N_{\text{tran}}(a)$ as the number of non-equivalent representative configurations a' that connect to a via some

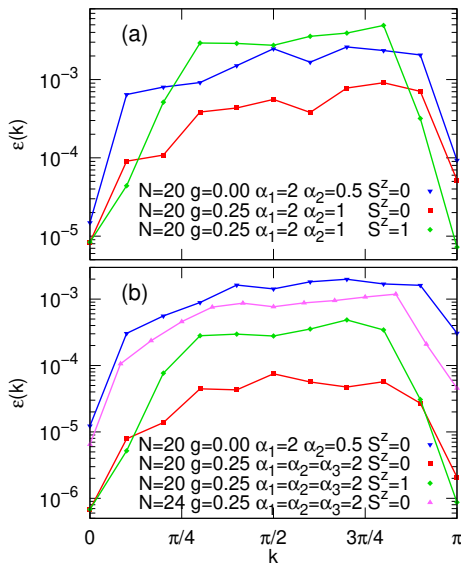


Figure 2. Relative error in energy $\epsilon(k) = \frac{E(k) - E_{\text{ED}}(k)}{|E_{\text{ED}}(k)|}$ as a function of the momentum k , observed at $g = 0$ and 0.25 , restricted to symmetry sectors $S^z = 0$ and 1 , using full summation over the symmetric subspace. (a) System size $N = 20$, using a 3-layer SeparateNet. (b) System sizes $N = 20$ and 24 , using 3-layer and 4-layer ComplexNets.

operator O , i.e., $\langle a'_k | O | a_k \rangle \neq 0$. In this paper, we choose $O = \sum_i (S_i^+ S_{i+1}^- + S_i^- S_{i+1}^+)$, which connects a and a' if any configuration in the equivalence class of a becomes one in the equivalence class of a' by flipping two nearest-neighbor spins. We equally propose all possible a' , such that $g(a, a') = 1/N_{\text{tran}}(a)$. The acceptance probability of the new representative configuration a' is then given by:

$$r(a, a') = \min \left(1, \frac{p(a') N_{\text{tran}}(a)}{p(a) N_{\text{tran}}(a')} \right). \quad (7)$$

Note that $N_{\text{tran}}(a)$ can be defined for an arbitrary symmetry group, which, together with $|\psi\rangle$, affects the acceptance rate.

Results. The Hamiltonian we select for demonstration is the frustrated spin-1/2 J_1 - J_2 antiferromagnetic Heisenberg model on the 1D chain with periodic boundary conditions, formulated as

$$H = J_1 \sum_{\langle i, j \rangle} \mathbf{S}_i \cdot \mathbf{S}_j + J_2 \sum_{\langle\langle i, j \rangle\rangle} \mathbf{S}_i \cdot \mathbf{S}_j, \quad (8)$$

where the summations are performed over the nearest-neighbor pairs $\langle i, j \rangle$ and the next-nearest-neighbor pairs $\langle\langle i, j \rangle\rangle$ respectively. Throughout this paper, we set $J_1 = 1$ and denote $g = J_2/J_1$. This simple model exhibits a diverse ground state phase diagram [28–30]. Specifically, its ground state is a Luttinger liquid (LL) for $g < g_{c1} \approx 0.2411$, an incommensurate spiral state for $g > g_{c2} \approx 0.5294$, and a valence bond solid (VBS) for $g_{c1} < g < g_{c2}$.

When $g < g_{c2}$, its ground states adhere to Marshall's sign rule, meaning the ground state becomes positive definite after a global spin rotation $\prod_{i \in B} S_i^z$ on the sublattice B .

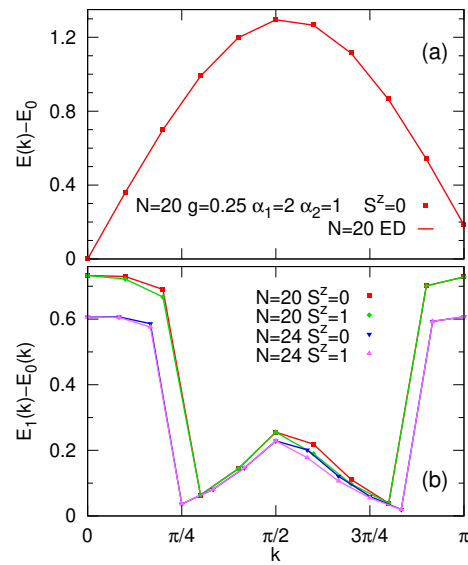


Figure 3. (a) Spinon dispersion as a function of the momentum k at $g = 0.25$ for system size $N = 20$, using a 3-layer SeparateNet and full summation over the symmetric subspace, compared to ED. The corresponding energy relative error is shown in Fig. 2 (a). (b) The lowest non-degenerate energy gap $\Delta(k) = E_1(k) - E_0(k)$ as a function of k , for system sizes $N = 20$ and 24 , restricted to symmetry sectors $S^z = 0$ and 1 , computed by ED.

Throughout this paper, we simulate the rotated Hamiltonian $H' = \prod_{i \in B} S_i^z H \prod_{i \in B} S_i^z$ instead.

The Hamiltonian is invariant under the translational symmetry T , the bond-mirror reflection symmetry P , and the spin inversion symmetry $Z = \prod_i S_i^x$. We also incorporate the total spin conservation $S^z = \sum_i S_i^z$. The ground state lies in the symmetry sector with quantum numbers $k = 0$ (or $k = \pi$), $p = 1$ (or $p = -1$), $z = 1$ (or $z = -1$), and $S^z = 0$ for a chain of length $N = 4n$ (or $N = 4n + 2$), where n is an integer, p is the reflection quantum number, and z is the spin inversion quantum number. To compute its low-energy dispersion when $k \neq 0$, we either set total spin $S^z = 1$, or set $S^z = 0$ and $z = -1$ for $N = 4n$ (or $z = 1$ for $N = 4n + 2$). We account for the reflection symmetry P at $k = \pi$ as well. The numbers of representative states N_{repr} for various system sizes N and quantum numbers (k, p, z, S^z) are listed in the supplementary material [26].

In Fig. 1, we illustrate the ground state energy as a function of optimization steps using Metropolis sampling for the $N = 20$ chain at couplings $g = 0.7$ and 1 , using a 4-layer ComplexNet whose number of hidden neurons $N_{h_i} = \alpha_i N$, and we configure $\alpha_i = 2$ for $i = 1, 2, 3$. The network has 4160 complex parameters in total. The relative errors compared to the exact ground state energy E_0 from ED, defined as $\epsilon = \frac{E - E_0}{|E_0|}$, are provided in Table I. As an ablation study, we compare the results to those with the same network and optimization strategy but without symmetrization, implemented using the NetKet package [31]. The symmetrization reduces the energy relative errors by approximately two orders of mag-

	$g = 0.7$		$g = 1$	
	symm.	w/o symm.	symm.	w/o symm.
ϵ	6.3×10^{-5}	1.3×10^{-3}	1.7×10^{-4}	8.2×10^{-3}

Table I. Relative errors of the ground state energy, defined as $\epsilon = \frac{E - E_0}{|E_0|}$, for the J_1 - J_2 chain of length $N = 20$ at $g = 0.7$ and 1, comparing the results with and without symmetrization.

nitude. Hyperparameters of the optimization are summarized in the supplementary material [26].

Next, we examine and compare the performances of SeparateNet and ComplexNet using full summation over the symmetric subspace. We begin by studying the low-energy dispersion as a function of the momentum k for a chain of length $N = 20$ at $g = 0$. We configure the ansatz as a 3-layer SeparateNet (or ComplexNet) with $\alpha_1 = 2$, $\alpha_2 = 0.5$, and 1210×2 real (or 1210 complex) parameters, restricted to the symmetry sectors $S^z = 0$ and $z = -1$. The simulation accuracy is indicated by energy relative errors, defined as $\epsilon(k) = \frac{E(k) - E_{ED}(k)}{|E_{ED}(k)|}$. The results with SeparateNet and ComplexNet are presented as blue triangles in Fig. 2 (a) and (b) respectively. Both networks achieve an accuracy on the order of 1×10^{-3} , which is slightly higher than the 3×10^{-4} achieved in Ref. [14]. This discrepancy is likely due to the parallel tempering scheme used in Ref. [14], which assists optimization in reaching the global minimum.

We proceed to study the low-energy dispersion at the coupling $g = 0.25$, which is close to the critical point $g_{c1} \approx 0.2411$ between the LL and the VBS. We investigate the impact of the symmetric subspace size on the variational energy by examining the degenerate states within different symmetry sectors. The low-energy dispersion of this model, i.e., the lowest triplet excitations at momentum k , are three-fold degenerate with quantum numbers $S^z = 0, \pm 1$ respectively. For the triplet with total spin $S^z = 0$, an additional spin inversion symmetry Z is applicable, with quantum number $z = -1$ for $N = 4n$. Consequently, the subspace for the $S^z = 0$ triplet is approximately half the size of those with $S^z = \pm 1$.

We apply a 3-layer SeparateNet with $\alpha_1 = 2$, $\alpha_2 = 1$, and 1680×2 real parameters to investigate the subspace size effect on a chain of length $N = 20$ at $g = 0.25$. The relative errors $\epsilon(k)$ as a function of k for $S^z = 0$ (red squares) and $S^z = 1$ (green diamonds) sectors are presented in Fig. 2 (a). For most momenta away from $k = 0$ and π , the $S^z = 0$ sector achieves energy accuracy approximately an order of magnitude better than the $S^z = 1$ sector, highlighting the advantage of a smaller variational subspace. For momenta near $k = 0$ and π , both sectors achieve high accuracy, and the accuracy in the $S^z = 0$ sector is comparable to that in the $S^z = 1$ sector.

To understand the behavior near $k = 0$ and π , we compare the spinon dispersion function $E(k) - E_0$ from the neural network and ED in Fig. 3 (a), and present the lowest non-degenerate energy gap $\Delta(k) = E_1(k) - E_0(k)$ from ED in Fig. 3 (b). The gap $\Delta(k)$ is particularly large near $k = 0$

and π , which shows the better isolation of eigenstates in the symmetric subspaces and improves the convergence speed of optimization.

We further increase the number of variational parameters by adopting a 4-layer ComplexNet with $\alpha_i = 2$ and 4160 complex parameters, to compute the dispersion of the $N = 20$ chain at $g = 0.25$, and present results from $S^z = 0$ and $S^z = 1$ sectors in Fig. 2 (b). The additional variational parameters significantly improve the accuracy, decreasing the relative errors by more than an order of magnitude, compared to the 3-layer SeparateNet in Fig 2 (a).

Finally, we present the relative error of dispersion for the $N = 24$ chain at $g = 0.25$, restricted to the symmetry sector $S^z = 0$ with $z = -1$, simulated using a 4-layer ComplexNet with $\alpha_i = 2$ and 5952 complex parameters. The simulation achieves a relative error of approximately 1×10^{-3} at the worst momentum, as shown by the magenta triangles in Fig. 2 (b).

Discussion and conclusions. Building on previous advancements of exact diagonalization (ED) [15–19] and symmetrization of neural quantum states (NQS) [14, 20], we have presented a method to evaluate and sample NQS within a significantly reduced symmetric subspace, where all basis vectors are orthogonal, non-local, and symmetric. By implementing a Metropolis sampling algorithm that satisfies detailed balance, our method enables large-scale simulations of symmetric NQS. Using feedforward neural networks (FFNN) as the basic architecture, we have tested our approach on the frustrated 1D J_1 - J_2 antiferromagnetic Heisenberg model. Our results demonstrate that, using the same network architecture and optimization strategy to find the ground state energy, a symmetric NQS achieves an accuracy approximately two orders of magnitude better than a conventional NQS without symmetry. Furthermore, simulations of low-energy dispersion across different symmetry sectors reveal that a smaller symmetric subspace significantly improves the variational energy, with the relative error reduced by one order of magnitude when the subspace size is reduced by half.

This framework holds immense potential for the accurate simulation of large-size many-body quantum Hamiltonians when combined with modern neural network models such as graph neural networks (GNN) [3–5] and transformers [8, 9]. Its ability to simulate excited states, in conjunction with spectroscopic methods [12, 32–34], offers a promising route for understanding subtle and intricate quantum phase transitions. We look forward to a more efficient implementation that integrates the symmetrization and the machine learning framework, which will not only advance the precision of quantum state simulations but also pave the way for exploring quantum phenomena in systems larger than previously feasible.

We would like to thank G. Carleo for helpful comments. S.-T.B. and L.W. are supported by the National Natural Science Foundation of China (NSFC) (Grant No. 12374150). P.Z. is supported by the NSFC (Grant No. 12047503, 12325501, and 12247104) and Project ZDRW-XX-2022-3-02 of the Chinese Academy of Sciences.

END MATTER

Energy gradients. We denote the complex variational parameters as θ_c in ComplexNet, and the real parameters in $A(a)$ and $\Phi(a)$ as θ_r and θ_i respectively in SeparateNet. Given the energy as the loss function, the gradient of energy with respect to θ in general (θ_c for ComplexNet, or θ_r and θ_i for SeparateNet) is expressed as:

$$\frac{\partial E}{\partial \theta} = \frac{\partial}{\partial \theta} \langle \psi | H | \psi \rangle. \quad (\text{S1})$$

After substituting $|\psi\rangle = \sum_a \psi(a)|a_k\rangle$, it becomes

$$\begin{aligned} \frac{\partial E}{\partial \theta} = & \left\langle \frac{\partial \ln \psi^*(a)}{\partial \theta} E_{\text{loc}}(a) + \frac{\partial \ln \psi(a)}{\partial \theta} E_{\text{loc}}^*(a) \right\rangle_a \\ & - 2\langle H \rangle_a \left\langle \frac{\partial \text{Re} \ln \psi(a)}{\partial \theta} \right\rangle_a, \end{aligned} \quad (\text{S2})$$

given that $\langle O \rangle_a = \frac{\sum_a |\psi(a)|^2 O(a)}{\sum_a |\psi(a)|^2}$, $E_{\text{loc}}(a) = \sum_{a'} \frac{\psi(a')}{\psi(a)} H_{a,a'}$, and $H_{a,a'} = \langle a_k | H | a'_k \rangle$. For ComplexNet, we have

$$\begin{aligned} \frac{\partial E}{\partial \theta_c} = & 2 \left\langle \frac{\partial \text{Re} \Psi(a)}{\partial \theta_c} \text{Re} E_{\text{loc}}(a) \right\rangle_a - 2\langle H \rangle_a \left\langle \frac{\partial \text{Re} \Psi(a)}{\partial \theta_c} \right\rangle_a \\ & + 2 \left\langle \frac{\partial \text{Im} \Psi(a)}{\partial \theta_c} \text{Im} E_{\text{loc}}(a) \right\rangle_a. \end{aligned} \quad (\text{S3})$$

Alternatively, for SeparateNet,

$$\begin{aligned} \frac{\partial E}{\partial \theta_r} = & 2 \left\langle \frac{\partial A(a)}{\partial \theta_r} \text{Re} E_{\text{loc}}(a) \right\rangle_a - 2\langle H \rangle_a \left\langle \frac{\partial A(a)}{\partial \theta_r} \right\rangle_a, \\ \frac{\partial E}{\partial \theta_i} = & 2 \left\langle \frac{\partial \Phi(a)}{\partial \theta_i} \text{Im} E_{\text{loc}}(a) \right\rangle_a. \end{aligned} \quad (\text{S4})$$

Eq. S3 and Eq. S4 bear resemblance to each other, thus exhibiting similar computational complexity. We have compared and discussed their performances in the main text.

Given the gradients obtained above, we further use stochastic reconfiguration (SR) [21–25] to regularize the optimization step for each variable. Following Refs. [14, 25], we consider updating the wavefunction by an infinitesimal step $\delta\theta$:

$$\psi(\theta + \delta\theta) = \psi(\theta) + \sum_{\theta} \delta\theta \frac{\partial \psi}{\partial \theta} = \psi(\theta) \left(1 + \sum_{\theta} \delta\theta \frac{\partial \ln \psi}{\partial \theta} \right). \quad (\text{S5})$$

The best solution $\delta\theta$ given by SR should minimize the distance between $\psi(\theta + \delta\theta)$ and the imaginary-time evolved wavefunction

$$\tilde{\psi}(\theta) = e^{-\tau H} \psi(\theta) = (1 - \tau H) \psi(\theta). \quad (\text{S6})$$

Their distance is defined as

$$d = \arccos \left(\sqrt{\frac{\langle \psi(\theta + \delta\theta) | \tilde{\psi}(\theta) \rangle \langle \tilde{\psi}(\theta) | \psi(\theta + \delta\theta) \rangle}{\langle \tilde{\psi}(\theta) | \tilde{\psi}(\theta) \rangle \langle \psi(\theta + \delta\theta) | \psi(\theta + \delta\theta) \rangle}} \right). \quad (\text{S7})$$

Let's define $d = \arccos \sqrt{1-x}$. Using Taylor expansion $\arccos \sqrt{1-x} \approx \sqrt{x}$ for small x , and keeping up to the second

order in τ and $\delta\theta$, we obtain a simplified x as follows:

$$x \approx \sum_{ij} \delta\theta_i^* S_{i,j} \delta\theta_j + \tau \left(\sum_i \delta\theta_i^* F_i + \sum_i F_i^* \delta\theta_i \right) + \tau^2 (\langle H^2 \rangle - \langle H \rangle^2), \quad (\text{S8})$$

where $S_{i,j} = \langle \frac{\partial \ln \psi^*}{\partial \theta_i} \frac{\partial \ln \psi}{\partial \theta_j} \rangle - \langle \frac{\partial \ln \psi^*}{\partial \theta_i} \rangle \langle \frac{\partial \ln \psi}{\partial \theta_j} \rangle$, and $F_i = \langle \frac{\partial \ln \psi^*}{\partial \theta_i} E_{\text{loc}} \rangle - \langle \frac{\partial \ln \psi^*}{\partial \theta_i} \rangle \langle H \rangle$. Minimizing Eq. S8 with respect to $\delta\theta_i^*$ results in the linear equations

$$S_{i,j} \delta\theta_j = -\tau F_i, \quad (\text{S9})$$

which can be solved by directly inverting the geometric matrix S , or by an iterative solver. For ComplexNet, the expression for F_i is

$$\begin{aligned} F_i = & \left\langle \frac{\partial \text{Re} \Psi(a)}{\partial \theta_c} \text{Re} E_{\text{loc}}(a) \right\rangle_a - \left\langle \frac{\partial \text{Re} \Psi(a)}{\partial \theta_c} \right\rangle_a \left\langle \text{Re} E_{\text{loc}}(a) \right\rangle_a \\ & + \left\langle \frac{\partial \text{Im} \Psi(a)}{\partial \theta_c} \text{Im} E_{\text{loc}}(a) \right\rangle_a - \left\langle \frac{\partial \text{Im} \Psi(a)}{\partial \theta_c} \right\rangle_a \left\langle \text{Im} E_{\text{loc}}(a) \right\rangle_a \\ & - i \left(\left\langle \frac{\partial \text{Im} \Psi(a)}{\partial \theta_c} \text{Re} E_{\text{loc}}(a) \right\rangle_a - \left\langle \frac{\partial \text{Im} \Psi(a)}{\partial \theta_c} \right\rangle_a \left\langle \text{Re} E_{\text{loc}}(a) \right\rangle_a \right) \\ & + i \left(\left\langle \frac{\partial \text{Re} \Psi(a)}{\partial \theta_c} \text{Im} E_{\text{loc}}(a) \right\rangle_a - \left\langle \frac{\partial \text{Re} \Psi(a)}{\partial \theta_c} \right\rangle_a \left\langle \text{Im} E_{\text{loc}}(a) \right\rangle_a \right), \end{aligned} \quad (\text{S10})$$

while for SeparateNet, F_i is simply $[\frac{\partial E}{\partial \theta_r}, \frac{\partial E}{\partial \theta_i}]$, where the brackets denote concatenation.

Sizes of symmetric subspaces. We summarize the sizes of the symmetric subspaces for the ground states and their low energy dispersions for chain lengths $N = 16, 20$, and 24 in Table S1. The ground states have the highest symmetry, with the quantum number set $(k, p, z, S^z) = (0, 1, 1, 0)$ for system sizes $N = 4n$. The lowest triplet gap locates at $(k, p, z, S^z) = (\pi, -1, -1, 0)$ and $(k, p, z, S^z) = (0, 1, N/A, \pm 1)$. Note that the unusual momentum quantum number $k = 0$ and reflection quantum number $p = 1$ for the lowest triplet with $S^z = \pm 1$ are caused by the global spin rotation $\prod_{i \in B} S_i^z$ on the sublattice B . Under the original Hamiltonian, the quantum number set would be $(k, p, z, S^z) = (\pi, -1, N/A, \pm 1)$. At other momenta $k \neq 0$ or π , the reflection symmetry is not applicable.

Optimization strategy. In the Monte Carlo (MC) simulation, we examine two typical couplings at $g = 0.7$ and 1 . For the system size $N = 20$, we set the number of samples per optimization step $n_{\text{sample}} = 4800$, the number of Markov chain steps to collect the samples $n_{\text{collect}} = 2N$, and the number of steps to discard before collecting the samples $n_{\text{discard}} = 10N$.

Starting from a random initialization, we observe that the symmetric NQS can easily get stuck in a local minimum caused by the dimer product state (Majumdar-Ghosh exact ground state at $g = 0.5$) when $g = 0.7$, whereas its non-symmetric counterpart does not. Therefore, we avoid this local minimum by initializing from a converged NQS at $g = 1$. This issue can also be circumvented if the number of samples n_{sample} is as large as $10N_{\text{repr}}$, or if directly enumerating the subspace.

N	$(0, 1, 1, 0)$	$(\pi, -1, -1, 0)$	$(0, 1, N/A, \pm 1)$	$(\pi/2, N/A, -1, 0)$	$(\pi/2, N/A, N/A, \pm 1)$
16	257	230	375	396	715
20	2518	2429	4262	4639	8398
24	28968	28648	52234	56275	104006

Table S1. Sizes of the symmetric subspaces for the ground states (Column 2), the lowest triplet states (Columns 3 and 4), and at $k = \pi/2$ (Columns 5 and 6), denoted by their quantum number sets (k, p, z, S^z) , for system sizes $N = 16, 20, \text{ and } 24$ respectively.

We utilize the Adam optimizer [35] with the first momentum $\beta_1 = 0.9$ and the second momentum $\beta_2 = 0.999$ throughout this work. When optimizing from a random initialization, we set the learning rate $\alpha = 10^{-3}$. When fine-tuning from a converged NQS, $\alpha = 10^{-5}$ is used instead. For MC sampling, we do not employ the SR method due to its time-consuming nature. For optimization with full summation, the SR method is employed for comparison. To prevent singular or very small eigenvalues of the geometric matrix S , we add an diagonal shift of size 10^{-3} to it. The linear equations are solved using the SciPy [36] function `gmres`, with the maximum number of iterations set to 40. The initial vector of the `gmres` function is always set to be F_i in Eq. S9.

* lingwangqs@zju.edu.cn

- [1] K. Choo, T. Neupert, and G. Carleo, Two-dimensional frustrated J_1 - J_2 model studied with neural network quantum states, *Phys. Rev. B* **100**, 125124 (2019).
- [2] A. Szabó and C. Castelnovo, Neural network wave functions and the sign problem, *Phys. Rev. Research* **2**, 033075 (2020).
- [3] D. Kochkov, T. Pfaff, A. Sanchez-Gonzalez, P. Battaglia, and B. K. Clark, Learning ground states of quantum Hamiltonians with graph networks, arXiv:2110.06390.
- [4] L. Yang, W. Hu, and L. Li, Scalable variational Monte Carlo with graph neural ansatz, arXiv:2011.12453.
- [5] Q.-H. Yu and Z.-J. Lin, Solving quantum many-particle models with graph attention network, *Chinese Phys. Lett.* **41**, 030202 (2024).
- [6] C. Fu, X. Zhang, H. Zhang, H. Ling, S. Xu, S. Ji, Lattice convolutional networks for learning ground states of quantum many-body systems, arXiv:2206.07370.
- [7] M. Hibat-Allah, M. Ganahl, L. E. Hayward, R. G. Melko, and J. Carrasquilla, Recurrent neural network wave functions, *Phys. Rev. Research* **2**, 023358 (2020).
- [8] L. L. Viteritti, R. Rende, and F. Becca, Transformer variational wave functions for frustrated quantum spin systems, *Phys. Rev. Lett.* **130**, 236401 (2023).
- [9] L. L. Viteritti, R. Rende, A. Parola, S. Goldt, and F. Becca, Transformer wave function for the Shastry-Sutherland model: Emergence of a spin-liquid phase, arXiv:2311.16889.
- [10] F. Verstraete, J. I. Cirac, Renormalization algorithms for quantum-many body systems in two and higher dimensions, arXiv:cond-mat/0407066.
- [11] C. Roth and A. H. MacDonald, Group convolutional neural networks improve quantum state accuracy, arXiv:2104.05085.
- [12] Y. Nomura and M. Imada, Dirac-type nodal spin liquid revealed by refined quantum many-body solver using neural-network wave function, correlation ratio, and level spectroscopy, *Phys. Rev. X* **11**, 031034 (2021).
- [13] T. Vieijra, C. Casert, J. Nys, W. De Neve, J. Haegeman, J. Ryckebusch, and F. Verstraete, Restricted Boltzmann machines for quantum states with non-abelian or anyonic symmetries, *Phys. Rev. Lett.* **124**, 097201 (2020).
- [14] K. Choo, G. Carleo, N. Regnault, and T. Neupert, Symmetries and many-body excitations with neural-network quantum states, *Phys. Rev. Lett.* **121**, 167204 (2018).
- [15] N. Laflorencie and D. Poilblanc, Simulations of pure and doped low-dimensional spin-1/2 gapped systems, *Lecture Notes in Physics* **645**, 227 (2004).
- [16] R. M. Noack and S. Manmana, Diagonalization and numerical renormalization-group-based methods for interacting quantum systems, *AIP Conf. Proc.* **789**, 93 (2005).
- [17] A. Weisse, H. Fehske, Exact diagonalization techniques, *Lecture Notes in Physics* **739**, 529 (2008).
- [18] A. Lauchli, Numerical simulations of frustrated systems, *Springer Ser. Solid-State Sci.* **164**, 481-511 (2011).
- [19] A. W. Sandvik, Computational studies of quantum spin systems, *AIP Conf. Proc.* **1297**, 135 (2010).
- [20] M. Bukov, M. Schmitt, and M. Dupont, Learning the ground state of a non-stoquastic quantum Hamiltonian in a rugged neural network landscape, *SciPost Physics* **10**, 147 (2021).
- [21] S. Sorella, Green function Monte Carlo with stochastic reconfiguration, *Phys. Rev. Lett.* **80**, 4558 (1998).
- [22] S. Sorella, Generalized Lanczos algorithm for variational quantum Monte Carlo, *Phys. Rev. B* **64**, 024512 (2001).
- [23] S. Sorella, M. Casula, and D. Rocca, Weak binding between two aromatic rings: Feeling the van der Waals attraction by quantum Monte Carlo methods, *The Journal of Chemical Physics*, **127**(1), 014105 (2007).
- [24] F. Becca and S. Sorella, *Quantum Monte Carlo Approaches for Correlated Systems*, Cambridge University Press, doi:10.1017/9781316417041 (2017).
- [25] M. Schmitt and M. Heyl, Quantum many-body dynamics in two dimensions with artificial neural networks, arXiv:1912.08828.
- [26] Energy gradients, stochastic reconfiguration (SR), sizes of the symmetric subspaces at various quantum number sets (k, p, z, S^z) for different system sizes N , and the hyperparameters of optimization are presented in the supplementary materials.
- [27] S. Chib and E. Greenberg, Understanding the Metropolis-Hastings algorithm, *The American Statistician* **49**, 327 (1995).
- [28] K. Nomura and K. Okamoto, Fluid-dimer critical point in $S = 1/2$ antiferromagnetic Heisenberg chain with next nearest neighbor interactions, *Phys. Lett. A* **169**, 433 (1992).
- [29] S. Eggert, Numerical evidence for multiplicative logarithmic corrections from marginal operators, *Phys. Rev. B* **54**, R9612 (1996).
- [30] S. Brehmer, A. K. Kolezhuk, H.-J. Mikeska, and U. Neugebauer, Elementary excitations in the gapped phase of a frustrated $S = 1/2$ spin ladder: From spinons to the Haldane triplet, *J. Phys.: Condens. Matter* **10**, 1102 (1998).

- [31] F. Vicentini, D. Hofmann, A. Szabó, D. Wu, C. Roth, C. Giuliani, G. Pescia, J. Nys, V. Vargas-Calderón, N. Astrakhansev, and G. Carleo, NetKet 3: Machine learning toolbox for many-body quantum systems, *SciPost Phys. Codebases*, 7 (2022).
- [32] L. Wang and A. W. Sandvik, Critical level crossings and gapless spin liquid in the square-lattice spin-1/2 J_1 - J_2 Heisenberg antiferromagnet, *Phys. Rev. Lett.* **121**, 107202 (2018).
- [33] J. Yang, A. W. Sandvik, and L. Wang, Quantum criticality and spin liquid phase in the Shastry-Sutherland model, *Phys. Rev. B* **105**, L060409 (2022).
- [34] L. Wang, Y. Zhang, and A. W. Sandvik, Quantum spin liquid phase in the Shastry-Sutherland model detected by an improved level spectroscopic method, *Chinese Phys. Lett.* **39**, 077502 (2022).
- [35] D. P. Kingma and J. Ba, Adam: A method for stochastic optimization, in 3rd International Conference on Learning Representations (ICLR) (2015).
- [36] SciPy 1.0: Fundamental algorithms for scientific computing in Python. *Nature Methods*, 17(3), 261-272 (2020).